Contents lists available at ScienceDirect

Proceedings of the Combustion Institute

journal homepage: www.elsevier.com/locate/proci





An easy but quantitative assessment of soot production rate and its dependence on temperature and pressure

Kevin Gleason a,b, Francesco Carbone a,c, Alessandro Gomez a,*

- a Department of Mechanical Engineering and Materials Science, Yale University, 9 Hillhouse Avenue, New Haven, CT 06520-8286, United States
- ^b GE Aerospace, 1 Neumann Way, Cincinnati, OH 45215, United States
- c School of Mechanical, Aerospace, and Manufacturing Engineering, University of Connecticut, 191 Auditorium Road, Unit 3139, Storrs, CT 06269-3139, United States

ARTICLE INFO

Keywords: Soot Counterflow High pressure Diffusion flame

ABSTRACT

The challenge of soot emission persists in combustion research due to the complexities of tracking the crucial stages of growth from fuel to soot nuclei and ultimately mature particles. Studying soot formation in flames often requires a sophisticated approach, involving detailed measurements of gaseous soot precursors and soot particles using multiple complementary diagnostics. On the other end of the spectrum of studies are simpler methods that capture the sooting tendency using a single index, akin to the cetane number in compression ignition engines and the octane number in spark ignition engines. This article seeks a middle ground, aiming to quantify the soot production rate while maintaining the simplicity of single-index characterizations. The approach involves establishing counterflow diffusion flames, measuring soot volume fraction through pyrometry, and accurately computing velocity and temperature profiles using a commercial code. These data allow for the quantification of the production rate from the soot governing equation. The methodology is applied to counterflow ethylene diffusion flames to examine the temperature dependence of the soot production rate across peak temperatures varying by several hundred degrees and pressures in the 1-32 atm range. The soot production rate per unit flame area falls within the range of 10^{-7} – 10^{-3} g/(cm²s) range and, when normalized with respect to the carbon flux, it ranges between 10^{-6} and nearly 10^{-2} . On a logarithmic scale, it linearly correlates with the peak temperature at a fixed pressure. Although this study deals only with flames of ethylene, the approach can be generalized to any fuel. The resulting database should be valuable not only for industry practitioners but also to the scientific community for the global validation of detailed soot models.

1. Introduction

Soot in flames has been characterized with drastically different approaches. On the one hand, empirical approaches, including smoke point, TSI Threshold Sooting Index (TSI) and Yield Sooting Index (YSI) have been used to make relative comparisons of sooting tendency among different fuels [1–7] and in the case of YSI to classify hundreds of compounds. Of these techniques, the smoke point height and its derivative, TSI, are definitely qualitative and account for both production in the core of the flame and oxidation in its upper part [8], which is dependent on the flame configuration. YSI should correlate better with soot production since it relies on the measurement of the maximum soot concentration before oxidation sets in. All of them have the convenience of being easy to implement and of relying on simple, inexpensive equipment for the necessary measurements. As a result, they are used

without the need for an elaborate infrastructure to pursue more quantitative soot research. The goal of labeling sooting tendency with a single number, analogous to the cetane number for Diesel fuels and octane number for gasoline, is eminently practical. It glosses over temperature and pressure dependence of the soot process and does not provide values of either production rate or yield as a percentage of carbon converted to soot. At the other end of the spectrum in the characterization of sooting flames lie detailed investigations attempting to track the entire evolution from parent fuel to soot particles via a host of complementary diagnostics for chemical speciation and particle size distribution, as in [9–11] and our own work [12–14].

The present contribution has an intermediate goal between providing a single-valued overall evaluation of sooting tendency and a detailed characterization of the soot process. As introduced in [15], it is a comparatively easy but quantitative alternative to the soot indices

E-mail addresses: kevin.gleason@yale.edu (K. Gleason), alessandro.gomez@yale.edu (A. Gomez).

https://doi.org/10.1016/j.proci.2024.105292

Received 4 December 2023; Accepted 2 June 2024

Available online 1 July 2024

1540-7489/© 2024 The Combustion Institute. Published by Elsevier Inc. All rights are reserved, including those for text and data mining, AI training, and similar technologies.

^{*} Corresponding author.

based on three components: a) a counterflow burner to enable the aerodynamic anchoring of one-dimensional diffusion flames, b) one-dimensional modeling of the flames and c) soot volume fraction measurements by pyrometry. The counterflow flame has been a benchmark for laminar flame studies and has been used extensively in soot studies [16]. Its one-dimensional nature facilitates the use of computational modeling with detailed chemical kinetics that has become a commodity in combustion research. Commercial and open-source codes (e.g., [17,18]) enable even researchers with a modest computational background to make use of these codes for research purposes. The main uncertainty lies in the chemical kinetic mechanism that is reliable and validated for aliphatic fuels but becomes progressively less reliable for aromatics, practical fuel surrogates and soot. Still, certain aspects of the model such as the velocity and temperature field are computed reliably in all cases so long as energy losses by radiation are either negligible or properly accounted for [19]. As to the soot volume fraction, pyrometry does not require any laser source and can be realized using a spectrally well-characterized and inexpensive digital camera [6,19,20]. As a result, it is within the experimental reach of virtually all combustion laboratories.

Using the computational model to obtain velocity and temperature profiles and pyrometry to obtain soot volume fraction profiles enables the computation of the soot production rate from the soot governing equation. As a demonstration of the method, we presented soot production rates of several gaseous aliphatics, such as methane, propane, ethylene, propene and acetylene, as well as their temperature dependence for a total of 26 flames [15]. We now extract temperature dependence and pressure dependence of the overall soot production rate for ethylene that has been the fuel of choice in fundamental soot studies for decades: temperature dependence is critical in any Arrhenius type of reactions, regardless if global or detailed; pressure is important since most practical applications of combustion occur at high pressures, with soot formation being exacerbated under these conditions. Yet, experiments on sooting flames at high pressures are relatively rare (e.g., [21-32]), since the experimental challenges are compounded in a high-pressure environment.

2. Methodology, experimental configuration, and computational approach

2.1. Methodology

The governing equation for soot in an axis-symmetric flow field yields the net soot production rate $\dot{\omega}_s^{m'}$, as

$$\dot{\omega}_{s}^{'''} = \frac{d}{dz}(\rho Y_{s} \cdot V_{ax}) + 2 \rho Y_{s} \cdot \frac{dV_{r}}{dr} + \frac{d}{dz}(\rho Y_{s} \cdot V_{th}) + \frac{d}{dz}(\rho Y_{s} \cdot V_{P})$$
 (1)

where ρ , V_{ax} , and dV_r/dr are the gas density, the axial velocity and radial velocity radial gradients (i.e., local strain rate) from the onedimensional model and the soot mass fraction $Y_s = (\rho f_v)/\rho$, is determined from knowledge of the local value of the gas density, ρ , from the modeling and the experimental measurements of fv. The net soot production rate on the left-hand side accounts, in principle, for both positive soot production, i.e. soot formation, ω_{sf}''' , and destruction via oxidation, $\omega_{so}^{'''}$, that is, $\omega_{s}^{'''}=\omega_{sf}^{'''}+\omega_{so}^{'''}$. However, if conditions are chosen so that soot forms on the fuel side near the flame and travels towards Gas Stagnation Plane (GSP) and Particle Stagnation Plane (PSP) in an environment that is free of both O2 and OH, there would be no oxidation. Therefore, ω_s would represent just the positive soot production rate, that is, $\omega_s''' = \omega_{sf}'''$. On the righthand side of Eq. (1) one finds the convective and diffusive (transport) terms of the soot governing equations with the last two terms as the contributions due to thermophoresis and Brownian diffusion, respectively.

Integrating Eq. (1) along the transverse direction provides the soot

production rate per unit flame surface area, Ω''_{sf} , as

$$\overset{"}{\underset{sf}{\Omega}} = \int\limits_{z_1}^{z_2} \omega_{sf} dz \cong \int\limits_{z_1}^{z_2} 2 \left[\rho Y_s \cdot \frac{d}{dr} (V_r) \right] dz, \tag{2}$$

where all other terms from the right-hand side of Eq. (1) cancel out once integration is carried out over an interval whose bounds, z_1 and z_2 , are outside the region along the flame axis where soot is detectable, that is where Y_s is identically zero. We use the approximate equality, since the last term in Eq. (2) relies on the *experimental* determination of Y_s .

In principle, the same approach could be applied to assess also the soot oxidation rate if we consider flames whose stoichiometric mixture fraction is greater than 0.5, with the flame positioned on the *fuel* side of the stagnation plane where soot oxidation is no longer negligible. However, the simplification leading to Eq. (2) would no longer be applicable and retaining all terms in Eq. (1) would necessitate the specification of Brownian diffusion that is particle size-dependent. As a result, further progress could be made only by adding additional measurements to determine the particle size distribution, which drastically complicates the task. Since retaining the simplicity of the methodology is of paramount importance, we will not explore this direction any further.

2.2. Burner geometry and flame selection

The burner consists of two identical converging nozzles oriented in counterflow configuration [32,33]. The internal diameter of each nozzle is 6.35 mm and the nozzles are separated by 10 mm. Both nozzles are surrounded by a nitrogen shroud to shield the flame from external disturbances. The counterflow configuration provides a one-dimensional flow field in the vicinity of the burner axis, as confirmed by digital camera photographs showing a locally flat flame. Flames are perturbed by varying the inert concentration in the feed streams to span a range of peak temperatures, but keeping constant the stoichiometric mixture fraction $Z_{st} = (1 + sY_{FF}/Y_{OO})^{-1} = 0.183$. Y_{FF} is the mass fraction of ethylene in the fuel stream and Y_{OO} is the mass fraction of oxygen in the oxidizer stream and s is the mass-based stoichiometric coefficient. Also, the global strain rate $a = 50s^{-1} = (V_{avg,f} + V_{avg,ox})/L$ is kept constant so that the position of the flame with respect to the gas stagnation plane and the overall residence time are constant in all flames. The selection of the stoichiometric mixture fraction is based on ensuring that there would be no significant oxidation of soot and $\omega_s'''=\omega_{sf}'''$. Under these conditions, the pressure is varied in the 1-8atm range while the peak temperature varied by several hundred degrees.

To access the higher pressure range 8–32atm and maintain the soot production rate at modest levels we choose different conditions resulting in higher values of Z_{st} and a lower global strain rate at 0.41 and $18s^{-1}$, respectively. Critical data for the two sets of flames are shown in Table 1, including fuel and oxygen mole fraction, with the complement to unity for nitrogen, average velocity at burner outlets, maximum computed flame temperature, adiabatic flame temperature and Z_{st} .

2.3. High pressure chamber

High-pressure experiments are conducted in a pressure chamber that is described in detail in [32]. The chamber main body is a $20 \times 20 \times 20 \text{cm}^3$ stainless steel cube with removable flanges on each side. The bottom of the chamber is equipped with a cylindrical extension that contains translation stages, a mounting system for the burner, and the fuel/oxidizer/inert inlet ports. Each lateral flange has a 13 mm thick and a 52mm-diameter BK7 window for optical access and each window is wrapped with an electric heater to prevent water condensation during operation. An auxiliary flow of nitrogen enters through the bottom of the chamber to pressurize and flush the chamber continuously during

Table 1Key parameters of examined flames.

$ \begin{array}{c ccccccccccccccccccccccccccccccccccc$	T_{ad}	Z_{st}
0.315 20.2 0.2181 19.9 1928 0.330 20.2 0.2289 19.8 1984 0.345 20.2 0.2396 19.8 2037 0.360 20.2 0.2504 19.8 2088 0.375 20.2 0.2612 19.8 2137 0.390 20.2 0.2720 19.8 2183 4atm 0.245 20.1 0.1685 19.9 1775 0.255 20.1 0.1756 19.9 1826 0.265 20.2 0.1826 19.8 1875	K	
0.330 20.2 0.2289 19.8 1984 0.345 20.2 0.2396 19.8 2037 0.360 20.2 0.2504 19.8 2088 0.375 20.2 0.2612 19.8 2137 0.390 20.2 0.2720 19.8 2183 4atm 0.245 20.1 0.1685 19.9 1775 0.255 20.1 0.1756 19.9 1826 0.265 20.2 0.1826 19.8 1875	2233	0.183
0.345 20.2 0.2396 19.8 2037 0.360 20.2 0.2504 19.8 2088 0.375 20.2 0.2612 19.8 2137 0.390 20.2 0.2720 19.8 2183 4atm 0.245 20.1 0.1685 19.9 1775 0.255 20.1 0.1756 19.9 1826 0.265 20.2 0.1826 19.8 1875	3 2269	0.183
4atm 0.265 20.2 0.2504 19.8 2088 0.375 20.2 0.2612 19.8 2137 0.390 20.2 0.2720 19.8 2183 0.245 20.1 0.1685 19.9 1775 0.255 20.1 0.1756 19.9 1826 0.265 20.2 0.1826 19.8 1875	1 2320	0.183
4atm 0.245 20.1 0.2612 19.8 2137 0.390 20.2 0.2720 19.8 2183 0.245 20.1 0.1685 19.9 1775 0.255 20.1 0.1756 19.9 1826 0.265 20.2 0.1826 19.8 1875	7 2367	0.183
4atm 0.390 20.2 0.2720 19.8 2183 0.245 20.1 0.1685 19.9 1775 0.255 20.1 0.1756 19.9 1826 0.265 20.2 0.1826 19.8 1875	3 2411	0.183
4atm 0.245 20.1 0.1685 19.9 1775 0.255 20.1 0.1756 19.9 1826 0.265 20.2 0.1826 19.8 1875	7 2450	0.183
0.255 20.1 0.1756 19.9 1826 0.265 20.2 0.1826 19.8 1875	3 2487	0.183
0.265 20.2 0.1826 19.8 1875	5 1974	0.183
	5 2027	0.183
0.275 20.3 0.1897 19.7 1923	5 2077	0.183
	3 2126	0.183
0.285 20.3 0.1968 19.7 1970	2173	0.183
0.295 20.3 0.2039 19.7 2016	5 2218	0.183
8atm 0.235 20.1 0.1615 19.9 1754	1922	0.183
0.245 20.1 0.1685 19.9 1809	9 1977	0.183
0.255 20.1 0.1756 19.9 1862	2 2031	0.183
0.265 20.1 0.1826 19.9 1914	1 2082	0.183
0.275 20.1 0.1897 19.9 1963	3 2133	0.183
8atm 0.114 7.4 0.2438 7.3 1838	3 2026	0.41
16atm 0.108 7.4 0.2309 7.3 1786	5 1957	0.41
32atm 0.100 7.4 0.2130 7.3 1697	7 1855	0.41

operation to prevent the accumulation of reactants and combustion gases. The exhaust port is located on the top flange and the top of the chamber is wrapped with copper tubing that circulates chilled water to prevent overheating. A back pressure regulator is installed on the exhaust line to regulate the chamber pressure.

2.4. Pyrometry

Soot volume fraction is measured via pyrometry using a Nikon D70 digital camera with a well characterized spectral response (400nm-700 nm) as described exhaustively in past work [19,20]. Flame flickering, as determined by the position of the flame chemiluminescence, is confined to within the pixel resolution. An Abel transform deconvolves the line-of-sight images of each color channel into two-dimensional fields and the ratio of any two Abel-transformed color channels is related to the intensity of radiation emitted through Planck's law. The soot volume fraction is calculated as

$$f_{\nu} = -\frac{\lambda_{e}}{\widetilde{K}_{ext}L_{p}} \ln \left\{ 1 - \in_{c}(\lambda_{e}) \frac{\tau_{c}S_{s}}{\tau_{s}S_{c}} \exp \left[-\frac{hc}{k_{B}\lambda_{e}} \left(\frac{1}{T_{c}} - \frac{1}{T_{s}} \right) \right] \right\}, \tag{3}$$

where λ_e , L_p , τ , and \widetilde{K}_{ext} are effective channel wavelength, pixel length, exposure time, and dimensionless extinction coefficient, respectively. We assume $\widetilde{K}_{ext} = 5.34 \pm 2.68$, accounting for the variability of the extinction coefficient with wavelength and soot maturity [19,34–38]. Subscripts 's' and 'c' refer to measurements on soot particles and to a light calibration source, respectively.

2.5. Computational approach

One-dimensional modeling of the flames is performed with ANSYS CHEMKIN-Pro [17] using the KM2 model [39] that showed good performance for flames of aliphatics. We account for multicomponent diffusion coefficients, thermal diffusion, and thermal radiation of CO, $\rm CO_2$, $\rm H_2O$, and $\rm CH_4$ in the optically thin limit. The KM2 mechanism was validated in a baseline flame up to 6-ring PAH [12].

3. Results and discussion

To orient the reader about the nature of these flames we show in ${f Fig.~1}$ the computed temperature profiles (left ordinate) as continuous

lines, the computed velocity profiles (right ordinate) as dashed lines and the soot volume fraction (symbols) for the 8-atm set of flames for a range of peak temperatures at a fixed stoichiometric mixture fraction, Z_{st}=0.183. Importantly, the computed temperatures had been previously validated by thermocouple measurements [12,19,20,23,33]. The temperature profiles are similar with peak readings at approximately z =0.5 mm, once the origin of the abscissa is chosen as the location of the GSP where the axial velocity component is null. As denoted by the peak temperature location, the flames are all on the oxidizer side at the same distance from the GSP because of the constancy of Z_{st}. Peak temperature changes are achieved by nitrogen dilution from both sides of the flame, tweaking the mole fractions of fuel and oxidizer and holding the velocity at the boundaries and, consequently, the strain rate constant. Soot appears immediately downstream of the location of peak temperature and grows monotonically in its path towards the PSP (right-to-left), spanning more than three orders of magnitude as the peak temperature varies between 1754 K and 1963 K.

The soot production rate from Eq. (2) is plotted in Fig. 2 versus the peak flame temperature, with curves parametrized as a function of pressure and stoichiometric mixture fraction. At a fixed pressure the production rate invariably increases with peak temperature but the increase is more accentuated at higher pressures showing a steeper slope. It correlates linearly with the peak flame temperature on a logarithmic scale denoting an exponential dependence. The exponential factors of each fitted line are 1.43E-2, 2.60E-2, 3.29E-2 (K^{-1}) for 1 atm, 4 atm, and 8 atm flames, respectively. A similar result would have been obtained using the adiabatic flame temperature in the abscissa. At fixed peak temperature and stoichiometric mixture fraction, the production rate increases drastically as pressure varies in the 1–8 atm range with the increase being accentuated at higher temperatures.

To shed light on the trends in Fig. 2, we revisit subsets of data in further details. First, we consider the case of $T_{max} \sim \! 1900$ K and $Z_{st} \! = \! 0.183$ and examine a change in pressure from 1 to 8 atm. Fig. 3 shows the temperature profiles in the top panel and the temperature-time history with overlapped profiles of soot volume fraction in the bottom panel. As the pressure increases, the flame become thinner and the peak temperature shifts slightly towards the GSP, but still remains firmly on the oxidizer side of the GSP for positive values of the abscissa.

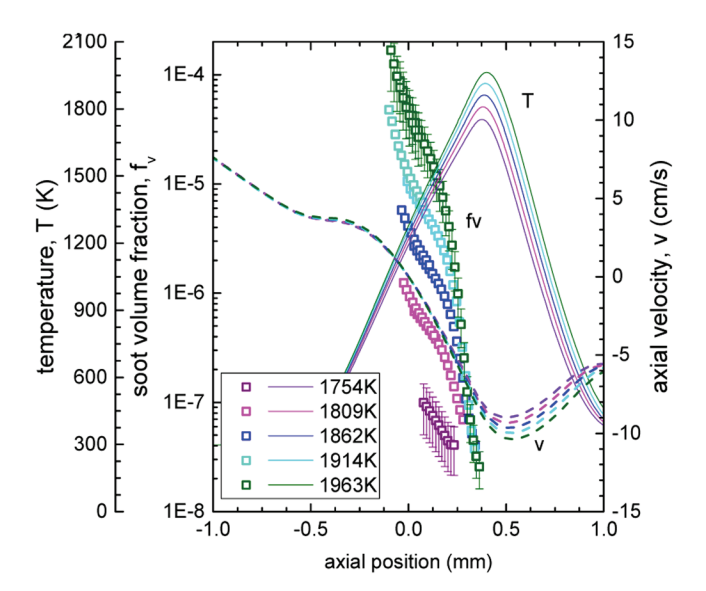


Fig. 1. Measured soot volume fraction (symbols) and computed temperature (solid lines) and axial velocity (dashed lines) for the 8-atm flame series. For presentation clarity, error bars in the volume fraction have been included only for the flames with the lowest (largest error) and highest (lowest error) T_{max} . The error bars include the uncertainty associated with three different color ratios and the soot dimensionless extinction coefficient.

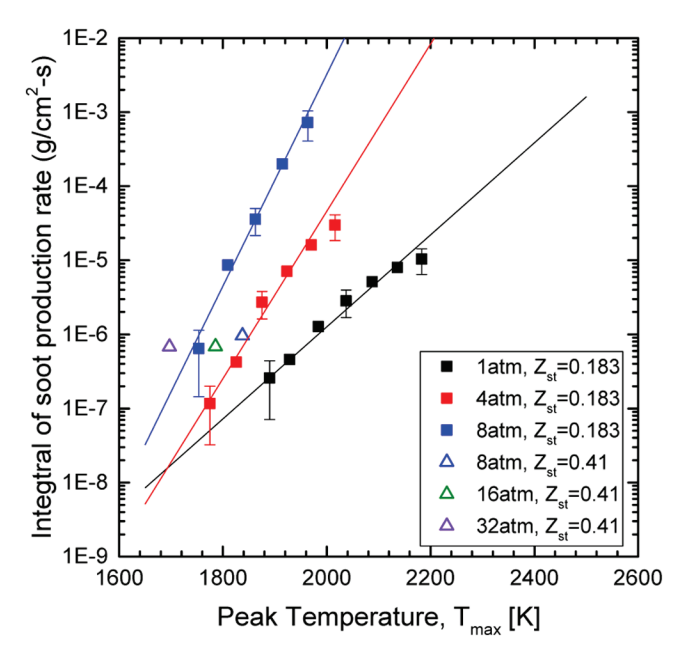


Fig. 2. C_2H_4 soot production rate per unit area versus peak flame temperature with data parametrized as a function of pressure and mixture fraction.

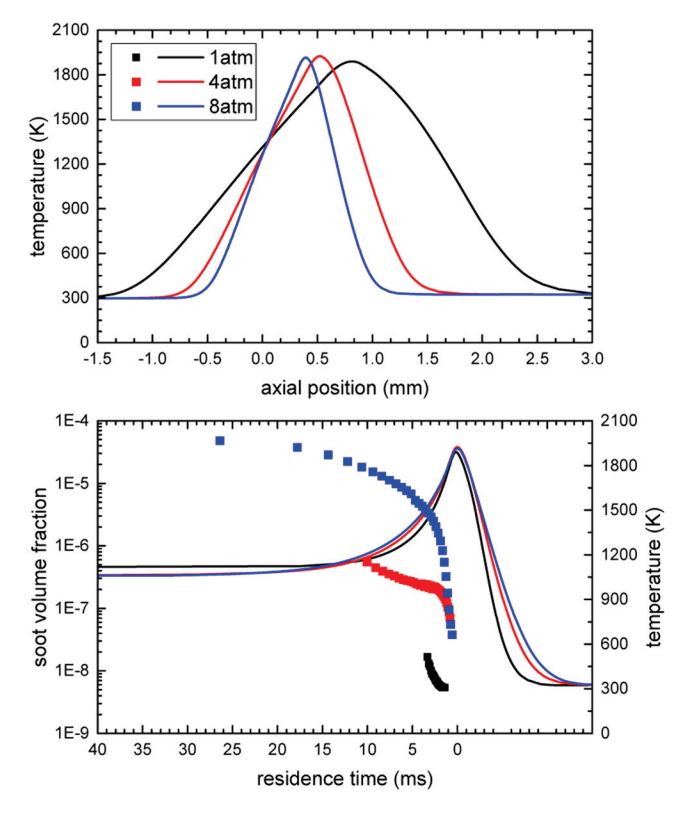


Fig. 3. Top panel: temperature versus axial position for $T_{max} \sim 1900~K$, Zst=0.183 and 1, 4 and 8 atm. Bottom panel: temperature (right ordinate) and soot volume fraction (left ordinate) versus convective residence time computed from the oxidizer side.

The temperature-time history profiles are obtained by integrating the inverse of the axial velocity in the transverse coordinate. The history curves are reasonably well overlapped as planned in the experiment design with constancy of both Z_{st} and strain rate, with small changes as pressure varies. The onset of soot occurs at approximately ~ 1 ms for all flames by setting t=0 at the position of T_{max} , which corresponds to a

computed temperature of 1700 K, 1835 K and 1875 K for the 1 atm, 4 atm and 8 atm flames, respectively. Soot volume fraction persists down to a temperature of 1450 K, 1200 K, and 1060 K, for 1 atm, 4 atm, and 8 atm flames, respectively. As reported in [23], the sharp differences in volume fraction spanning more than three orders of magnitude are the result of primarily a concentration effect on bimolecular collision rates increasing soot nucleation rate and PAH dimerization rate. Changes in pressure and temperature tend to be progressively more consequential on aromatics of increasing molecular weight and soot, as discussed in further details in [23].

Two mechanisms appear to account for soot production [19,20]: the classic high-temperature one near the flame with progressive dehydrogenation as particles move away from the flame and a low-temperature mechanism, further downstream and at later times. There are differences in soot production rate in the low temperature regime with increasing contribution at high pressure, but the integrated production rate in Fig. 2 accounts for both.

The next comparison set is for the flame in the high pressure 8–32 atm range, with higher Z_{st} and lower strain rate as well as longer residence time, as shown in Fig. 4. Conditions were chosen to ensure compatibility with diagnostics relying on sampling of the gas via capillary probe and multicolor pyrometry, resulting in comparably light soot loading. To that end, as the pressure was raised in twofold increments the ensuing pressure-induced increase in soot formation was offset with a $\sim \! 100$ K decrease in peak temperature in the soot forming zone [24]. As a result, the temperature time history changes and, as the pressure is raised, unlike the $Z_{st} \! = \! 0.183$ flames, the integrated soot production rate actually decreases (Fig. 2). The decrease in peak temperature, in fact, outweighs the pressure increase with respect to soot formation. The onset of soot appears at approximately 1 ms after setting the time origin at the position of T_{max} and at temperatures of 1800 K, 1770 K, and 1685 K as the pressure is raised, with soot persisting as

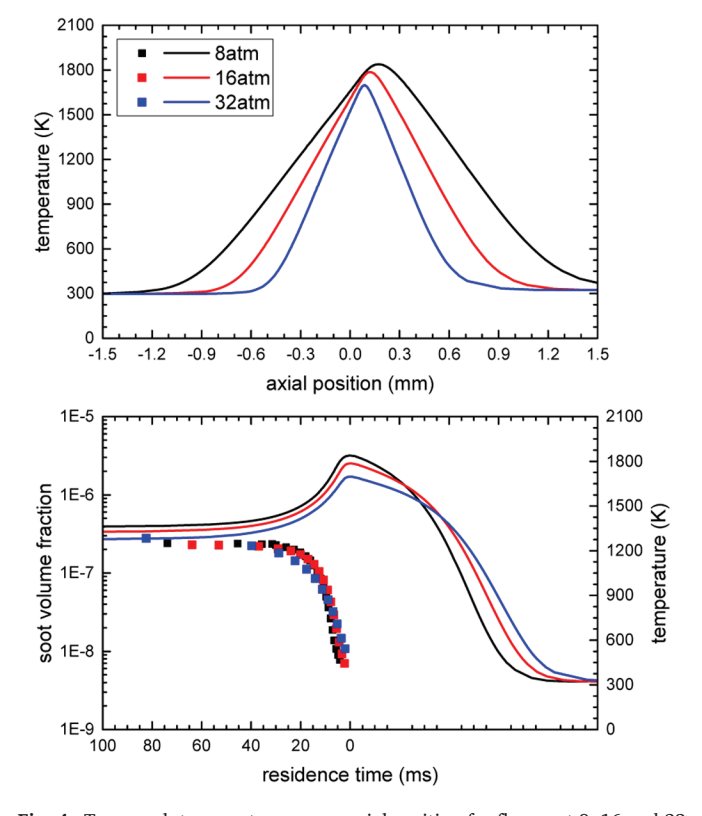


Fig. 4. Top panel: temperature versus axial position for flames at 8, 16 and 32 atm and $Z_{\rm st}$ =0.41. Bottom panel: temperature (right ordinate) and soot volume fraction (left ordinate) versus convective residence time computed from the oxidizer side.

temperature decreases to approximately 1300 K. The profiles of soot volume fraction appear to be invariant to the pressure change in the high-temperature region near the flame. This is consistent with the observation that benzene and other key aromatic precursors are measured to be independent of pressure [24]. Also in this case two mechanisms of soot formation are at work, the classic high-temperature one near T_{max} and a low-temperature mechanism, further downstream towards the GSP and at later times, with increasing contributions of the latter at high pressure.

Fig. 5 compares two flames at the same pressure of 8 atm and approximately the same peak temperature $T_{max}\sim1850$ K, to evidence the effect of changes in mixture fraction and strain rate. We notice a clear shift in the flame position closer to the GSP as the mixture fraction increases from 0.183 to 0.41 and the much expanded temperature-time history in the case with higher Z_{st} which is also characterized by a lower strain rate. With the usual selection of t=0 at the location of T_{max} for both flames, the corresponding onset of soot is within 2 ms, and can be treated the same within experimental uncertainty. Soot persists down to a temperature of 1140 K and 1370 K for the lower and higher Z_{st} flames, respectively. Importantly, there is a drastic decrease of the soot production rate that appears to be correlated with the lower content of aromatics that are precursors to soot [20,24,33].

The discussion of Figs. 3-5 demonstrates the advantage of analyzing data and rationalizing results using computation work within easy reach of most researchers. This is a bonus of the advocated approach to a quantitative assessment of soot production rate by comparison with alternative indices of sooting tendency whose interpretation is necessarily more qualitative.

It is instructive to obtain a nondimensional soot yield, similar to TSI and YSI, and account for the change in carbon flux with fuel flow rate. To do so, we nondimensionalize Eq. (2) as

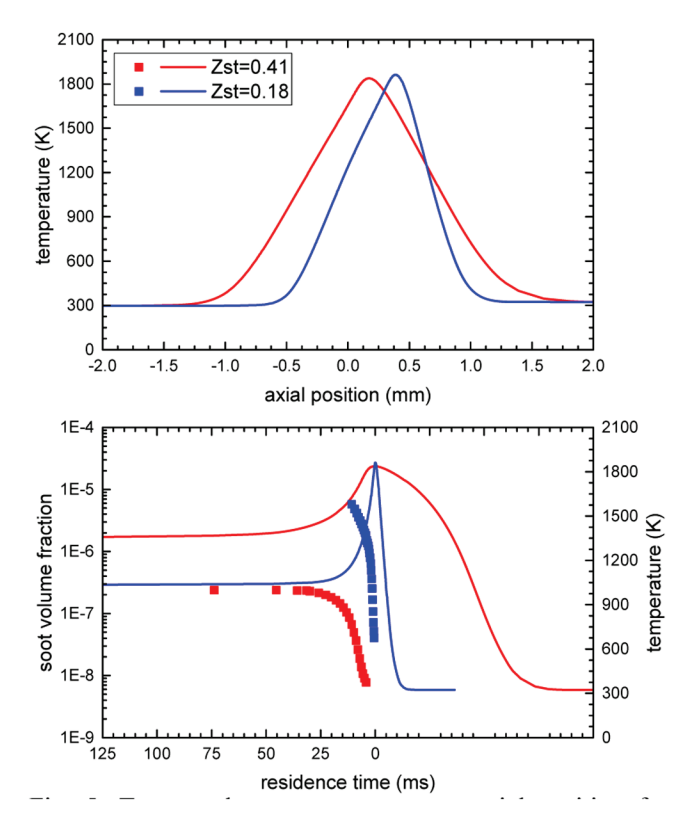


Fig. 5. Top panel: temperature versus axial position for flames at 8 atm and peak temperature $T_{\text{max}}{\sim}1850~\text{K}$ at different Z_{st} . Bottom panel: temperature (right ordinate) and soot volume fraction (left ordinate) versus convective residence time computed from the oxidizer side.

$$\widetilde{\Omega}_{s} = \frac{\Omega_{sf}'' A_{n}}{m_{r}} , \qquad (4)$$

where A_n is the burner nozzle area and m_c is the carbon mass flow rate (mass flow rate multiplied by the mass fraction of carbon atoms in the fuel stream) for each flame, resulting in a soot yield that is plotted in Fig. 6 as a function of the peak temperature. This yield represents soot production rate per flow rate of carbon atoms revealing how much of that carbon is converted into soot. The yield ranges between 10^{-6} and slightly more than 10^{-2} with a similar temperature dependence as the production rate in Fig. 2. This nondimensional representation is potentially more useful to extract information of broader applicability than the specific counterflow flames under consideration.

This proof-of-concept of a simple but quantitative assessment of soot production rate is focused on C₂H₄. Extension to other fuels, especially vapors of liquids, blends and (surrogates of) practical fuels are eminently feasible. For these studies doping a baseline nonsooting flame of, say, methane/air, with trace amounts of prevaporized fuels of interest would be implemented as in [6]. This approach is particularly useful since the baseline gaseous flame environment would provide a well-defined reactor in terms of fixed temperature-time history, major species, primary H—OH—O radical pool and possibly intermediate small aliphatic fragments, while the perturbation on these variables associated with the doping of fuels of different sooting tendencies would be negligible so long as the soot loading is modest. Indeed, the doping approach was used in much of our earlier work with liquid fuels in counterflow flames [40-43]. As a result, one can select conditions of practical relevance at least in the baseline flame and perturb it with small amount of fuels with high sooting tendency.

4. Conclusions

The presented work introduces a methodology for assessing the quantitative production rates of soot in ethylene diffusion flames, covering a range of peak temperatures spanning several hundred degrees and pressures from 1 to 32 atm. This method involves measuring volume fraction through pyrometry and computing velocity and temperature profiles using a commercial code in a counterflow diffusion flame configuration. Measurements indicate production rates varying

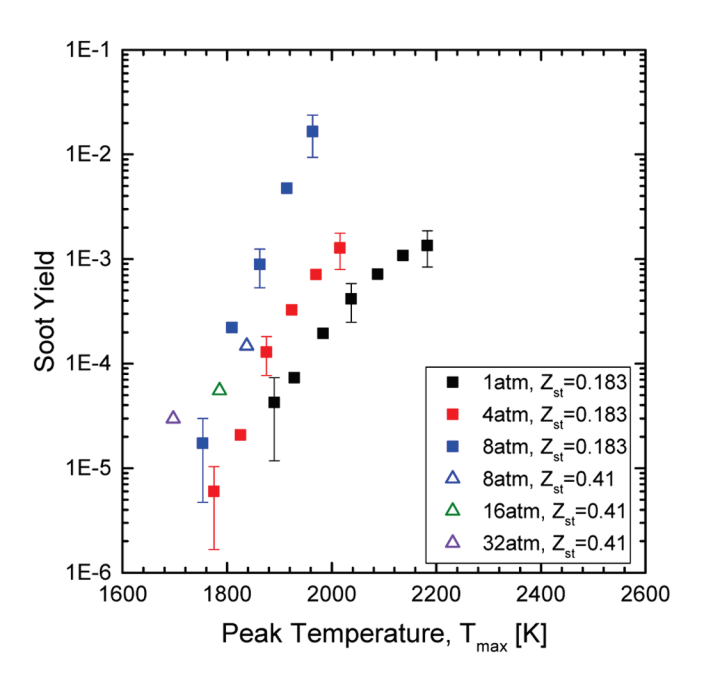


Fig. 6. Soot yield versus peak flame temperature with data parametrized as a function of pressure and mixture fraction.

from 10^{-7} to 10^{-3} g/(cm²s). Normalizing these rates to the carbon flow rate results in a soot yield ranging from 10^{-6} to 10^{-2} . At a constant pressure, the production rate exhibits an exponential dependence on temperature, that is more pronounced at the highest pressure within the 1-8 atm range for flames with a stoichiometric mixture fraction of 0.183. Extending the pressure to the 8-32 atm range with an increased stoichiometric mixture fraction of 0.41 necessitated a reduction in peak temperature through dilution to maintain a moderate soot load. Under these conditions, the pressure- and temperature dependence are less prominent, with the temperature effect overshadowing the pressure effect, leading to a reduction in soot production rate as the pressure quadruples and the peak temperature concurrently decreases by 243 K. The computation of temperature and velocity field, that is nowadays reliable with most software, provides a convenient means to interpret and rationalize the computed soot production rate by examining the temperature-time history of the soot evolution in the flame.

Novelty and significance statement

The novelty of the work is the introduction of a quantitative assessment of soot formation rate requiring a simple experimental measurement of soot volume fraction by pyrometry and the use of (open-source) computational modeling of counterflow flames. The method lends itself to establishing the pressure and temperature dependence of the production rate with ease.

Authors' contributions

AG conceived the study, supervised the data analysis and wrote the article: KG performed the experimental work, analyzed data and edited the article; FC supervised the experimental work and data analysis.

Declaration of competing interest

The authors declare that they have no known competing financial interests or personal relationships that could have appeared to influence the work reported in this paper.

Acknowledgments

The authors acknowledge the support of the National Science Foundation (CBET-1853150) and Yale University. F.C acknowledges also the support of the National Science Foundation (CBET-2013382).

References

- R.L. Schalla, G.E. McDonald, Variation in smoking tendency among hydrocarbons of low molecular weight, Ind. Eng. Chem. 45 (1953) 1497–1500.
- [2] Y. Yang, A.L. Boehman, R.J. Santoro, A study of jet fuel sooting tendency using the threshold sooting index (TSI) model, Combust. Flame. 149 (2007) 191–205.
- [3] H.F. Calcote, D.M. Manos, Effect of molecular structure on incipient soot formation, Combust. Flame. 49 (1983) 289–304.
- [4] L. Li, P.B. Sunderland, An improved method of smoke point normalization, Combust. Sci. Technol. 184 (2012) 829–841.
- [5] C.S. McEnally, L.D. Pfefferle, Improved sooting tendency measurements for aromatic hydrocarbons and their implications for naphthalene formation pathways, Combust, Flame, 148 (2007) 210–222.
- [6] D.D. Das, C.S. McEnally, T.A. Kwan, J.B. Zimmerman, W.J. Cannella, C.J. Mueller, L.D. Pfefferle, Sooting tendencies of diesel fuels, jet fuels, and their surrogates in diffusion flames, Fuel 197 (2017) 445–458.
- [7] D.D. Das, P.C. St. John, C.S. McEnally, S. Kim, L.D. Pfefferle, Measuring and predicting sooting tendencies of oxygenates, alkanes, alkenes, cycloalkanes, and aromatics on a unified scale. Combust. Flame, 190 (2018) 349–364.
- [8] A. Gomez, I. Glassman, Quantitative comparison of fuel soot formation rates in laminar diffusion flames, Proc. Combust. Inst. 21 (1988) 1087–1095.
- [9] K.C. Smyth, J.H. Miller, R.C. Dorfman, W.G. Mallard, R.J. Santoro, Soot inception in a methane/air diffusion flame as characterized by detailed species profiles, Combust. Flame, 62 (1985) 157–181.
- [10] M. Hellmuth, F. Cameron, S. Faller, L. Schmuckert, B. Chen, Y. Ren, H. Pitsch, Synergistic effect on PAH and soot formation in ethylene counterflow diffusion flames by the addition of 1, 3-dioxolane-a bio-hybrid fuel, Proc. Combust. Inst. 39 (2023) 899–908.

- [11] H.Q. Do, A. Faccinetto, L.S. Tran, P. Desgroux, L. Gasnot, A. El Bakali, X. Mercier, Hydrogen as a fuel additive in laminar premixed methane flames: impact on the nucleation and growth of soot particles, Fuel 315 (2022).
- [12] K. Gleason, F. Carbone, A.J. Sumner, B.D. Drollette, D.L. Plata, A. Gomez, Small aromatic hydrocarbons control the onset of soot nucleation, Combust. Flame. 223 (2021) 398–406.
- [13] F. Carbone, K. Gleason, A. Gomez, Probing gas-to-particle transition in a moderately sooting atmospheric pressure ethylene/air laminar premixed flame. Part I: gas phase and soot ensemble characterization, Combust. Flame. 181 (2017) 315–328.
- [14] F. Carbone, S. Moslih, A. Gomez, Probing gas-to-particle transition in a moderately sooting atmospheric pressure ethylene/air laminar premixed flame. Part II: molecular clusters and nascent soot particle size distributions, Combust. Flame. 181 (2017) 329–341.
- [15] K. Gleason, A. Gomez, A simple method for the quantitative assessment of soot production rate, Combust. Flame. 258 (2023) 113043.
- [16] Y. Wang, S.H. Chung, Soot formation in laminar counterflow flames, Prog. Energy Combust. Sci. 74 (2019) 152–238.
- [17] OpenSmoke++, https://www.opensmokepp.polimi.it/.
- [18] ANSYS CHEMKIN-Pro Release R2, (2019).
- [19] K. Gleason, F. Carbone, A. Gomez, Effect of temperature on soot inception in highly controlled counterflow ethylene diffusion flames, Combust. Flame. 192 (2018) 283–294.
- [20] K. Gleason, F. Carbone, A. Gomez, Pressure and temperature dependence of soot in highly controlled counterflow ethylene diffusion flames, Proc. Combust. Inst. 37 (2019) 2057–2064.
- [21] A.E. Karatas, O.L. Gulder, Soot formation in high pressure laminar diffusion flames, Prog. Energy Combust. Sci. 38 (2012) 818–845.
- [22] S.A. Steinmetz, T. Fang, W.L. Roberts, Soot particle size measurements in ethylene diffusion flames at elevated pressures, Combust. Flame. 169 (2016) 85–93.
- [23] K. Gleason, F. Carbone, A. Gomez, PAHs controlling soot nucleation in 0.101—0.811MPa ethylene counterflow diffusion flames, Combust. Flame. 227 (2021) 384–395.
- [24] K. Gleason, F. Carbone, A. Gomez, Spatially resolved measurements of soot and gaseous precursors in ethylene counterflow diffusion flames up to 32atm, Proc. Combust. Inst. 38 (2021) 2517–2524.
- [25] M. Commodo, P.H. Joo, G. De Falco, P. Minutolo, A. D'Anna, O.L. Gulder, Raman Spectroscopy of Soot Sampled in High-Pressure Diffusion Flames, Energy and Fuels 31 (2017) 10158–10164.
- [26] M. Gu, F. Liu, J.L. Consalvi, Ö.L. Gülder, Effects of pressure on soot formation in laminar coflow methane/air diffusion flames doped with n-heptane and toluene between 2 and 8 atm, Proc. Combust. Inst. 38 (2021) 1403–1412.
- [27] S. Liang, Z. Li, J. Gao, X. Ma, H. Xu, S. Shuai, PAHs and soot formation in laminar partially premixed co-flow flames fuelled by PRFs at elevated pressures, Combust. Flame. 206 (2019) 363–378.
- [28] X. Xue, P. Singh, C.J. Sung, Soot formation in counterflow non-premixed ethylene flames at elevated pressures, Combust. Flame. 195 (2018) 253–266.
- [29] H.M.F. Amin, A. Bennett, T.F. Guiberti, W.L. Roberts, Measurement of soot volume fraction in counterflow diffusion flames up to 10 Atm using optical diagnostics, Combust. Sci. Technol. (2023) 1–16.
- [30] B.G. Sarnacki, H.K. Chelliah, Sooting limits of non-premixed counterflow ethylene/ oxygen/inert flames using LII: effects of flow strain rate and pressure (up to 30 atm), Combust. Flame. 195 (2018) 267–281.
- [31] J. Li, H. Li, J. Shang, Z. Gan, Experimental evaluation of dimensionless extinction coefficient of soot in co-flow laminar diffusion flames at elevated pressures, Combust. Flame, 252 (2023) 112751.
- [32] L. Figura, A. Gomez, Laminar counterflow steady diffusion flames under high pressure (P<3MPa) conditions, Combust. Flame. 159 (2012) 142–150.</p>
- [33] K. Gleason, Soot Formation in High-Pressure Counterflow Flames, Yale University, 2020.
- [34] J. Simonsson, N.-E. Olofsson, S. Török, P.-E. Bengtsson, H. Bladh, Wavelength dependence of extinction in sooting flat premixed flames in the visible and nearinfrared regimes, Appl. Phys. B Lasers Opt. 119 (2015) 657–667.
- [35] T.C. Williams, C.R. Shaddix, K.A. Jensen, J.M. Suo-Anttila, Measurement of the dimensionless extinction coefficient of soot within laminar diffusion flames, Int. J. Heat Mass Transf. 50 (2007) 1616–1630.
- [36] F. Liu, J. Yon, A. Fuentes, P. Lobo, G.J. Smallwood, J.C. Corbin, Review of recent literature on the light absorption properties of black carbon: refractive index, mass absorption cross section, and absorption function, Aerosol Sci. Technol. 54 (2020) 33–51.
- [37] H. Chang, T.T. Charalampopoulos, Determination of the wavelength dependence of refractive indices of flame soot, Proc. R. Soc. London A Math. Phys. Eng. Sci. 430 (1990) 577–591.
- [38] D.R. Snelling, F. Liu, G.J. Smallwood, Ö.L. Gülder, Determination of the soot absorption function and thermal accommodation coefficient using low-fluence LII in a laminar coflow ethylene diffusion flame, Combust. Flame. 136 (2004) 180–190.
- [39] Y. Wang, A. Raj, S.H. Chung, A PAH growth mechanism and synergistic effect on PAH formation in counterflow diffusion flames, Combust. Flame. 160 (2013) 1667–1676.
- [40] S. Jahangirian, C.S. McEnally, A. Gomez, Experimental study of ethylene counterflow diffusion flames perturbed by trace amounts of jet fuel and jet fuel surrogates under incipiently sooting conditions, Combust. Flame. 156 (2009) 1799–1809.
- [41] H. Bufferand, L. Tosatto, B.La Mantia, M.D. Smooke, A. Gomez, Experimental and computational study of methane counterflow diffusion flames perturbed by trace

- amounts of either jet fuel or a 6-component surrogate under non-sooting conditions, Combust. Flame. 156 (2009) 1594–1603.

 [42] F. Carbone, A. Gomez, The structure of toluene-doped counterflow gaseous diffusion flames, Combust. Flame. 159 (2012) 3040–3055.
- [43] K. Gleason, A. Gomez, Detailed study of the formation of soot precursors and soot in highly controlled ethylene(/toluene) counterflow diffusion flames, J. Phys. Chem. A. 127 (2023) 276–285.